Mechanical Engineering - Engineering Fluid Dynamics

Conceptual design & experimental validation of Mars helicopter

Author:

Martijn Wilpshaar
s1456679

Organization:

Japanese Aerospace Exploration Agency

External supervisor:

Prof. A. Oyama

Internal supervisor:

Prof. H.W.M. Hoeijmakers

February 18, 2019

Abstract

The Japanese Aerospace Exploration Agency (JAXA) is planning a mission to Mars where a helicopter will be used to do research in caves and pit craters. The caves are interesting because of the higher possibility of finding life. The temperature is moderate and steady and there is less radiation compared to Mars' surface. The pit craters are interesting because these show the geological history of Mars. In this report, the feasibility of completing these missions with a helicopter is questioned. To answer this question, a conceptual design program has been programmed. This program computes the optimal blade pitch and chord distribution and computes the mass decomposition and maximum flight time. The input values and used equipment of this conceptual design program follow from previous research performed by JAXA. To compute the thrust and power, the Blade Element Momentum Theory is applied with 3D corrections. The final designed helicopter has a total mass of about 8kg and a maximum flight time of about 2200s, giving it enough time to complete the proposed missions. The use of the Blade Element Momentum Theory is validated for the low Reynolds number regime using hovering experiments in a vacuum tank. This has been done for two airfoils (flat plate& thin angular airfoil) and the results confirm the validity of the theory. However, for pitch angles larger than 20deg, the theoretic and experimental results differ which is caused by stall of the blades that is not taken into account in the theory.

Acknowledgements

Foremost, I would like to express my gratitude to my supervisor Prof. A.Oyama. His guidance helped me in doing the research and writing of this report.

Besides my supervisor in Japan, I would like to thank my supervisor in the Netherlands, Prof. H.W.M.Hoeijmakers for arranging the oppurtunity to do research at JAXA.

My sincere thanks also goes to Ms.Koh and Ms.Aoki for the good collaboration on the research and their help during the experiments.

I would also like to thank the other lab members that made me feel welcome and comfortable both in their lab as in their country.

Contents

Chapter 1

Introduction

In order to get a better understanding of the planet Mars and research the possibility of life, flying on Mars has been proposed in the past. Rovers, landers and satellites are already present on Mars. Rovers and landers can capture the surroundings into great detail but lack the ability to travel (long) distances and are also not capable of exploring rough terrain. The satellites, in contrary, have the ability to explore the whole planet of Mars but lack the ability of providing high detailed characteristics of the surroundings. Flying on Mars can fill the gap between the rovers/landers on one hand and satellites on the other hand in terms of resolution and distance covered. In the past, several conceptual studies have been performed on the possibility of flying on Mars using balloons [1, 2], fixed-wing airplanes [3–5] and rotor craft [6–9]. Balloons cannot follow a specified path and need to be extremely lightweight because of the thin atmosphere as well as strong enough for the various storms that are present on Mars. Fixed-wing airplanes need to maintain high speeds in order to generate enough lift in the thin atmosphere. A rotor craft would be the perfect machine for flying on Mars. It has the ability to hover at interesting places and can take-off and land vertically without the need of a runway.

1.1 Atmospheric differences

A lot of conceptual studies for rotor craft have been made. The reason these studies are still concepts is that the atmosphere at Mars is harsh for flying. The most important atmospheric differences between the earth and mars are listed in Table 1.1. The equipment has to cope with low temperatures and high amounts of radiation. However, the biggest problems are aerodynamically. With the low density and low speed of sound present on Mars, the helicopter will fly in a completely different Reynolds and Mach regime that is seen on earth. For a small helicopter, the Reynolds regime will be about $\mathcal{O}(10^3) - \mathcal{O}(10^4)$. Within this range, low lift over drag values are encountered because of the different flow separation phenomena that are active [10]. The lower gravitational constant is an advantage for flying on Mars.

Table 1.1: Atmospheric differences Earth & Mars

Parameter	Earth	Mars	Unit
Average surface density	1.225	0.0155	$[kg/m^3]$
Average surface Temperature	14	-60	$[°C]$
Speed of Sound	343	220	$[m/s]$
Gravitational constant	9.81	3.71	$[m/s^2]$

1.2 Proposed JAXA mission

Mars its surface is a severe place for living organism. There are high amounts of radioactive radiation as well as ultraviolet radiation. Furthermore, the temperature is low and fluctuates a lot. However, Mars is also rich of caves. Inside these caves, there is no radioactive or ultraviolet radiation present. Also, the temperature can be moderate without too much fluctuations. This is why within caves the highest possibility of life is expected. Another advantage for flying in these caves is that the ambient density is slightly higher compared to the average surface density of Mars.

Therefore, the proposed JAXA mission is to explore the caves on Mars. Within this mission, also the idea for exploring pit craters is proposed. Pit craters show the interesting geological history of Mars. For this mission, the idea of a small rotor craft is proposed that will be accompanied by a large rover ($\sim 50kg$). The tasks of the rotor craft include taking off of the rover, flying within the crater/cave while making pictures and returning to the rover. The first step in the design is the choice of equipment, choice of landing site and rotor configuration. This has been chosen by JAXA in previous reserach [11]. Because of the atmosphere difference, the aerodynamic design is a key factor in the overall design and therefore is handled next in this work.

1.3 Conceptual design program

In previous research, a coaxial rotor configuration has been chosen. This is chosen because of the limitations in tip speed, because of Mars' lower speed of sound. Two times two blades are chosen because of the increased Reynolds number involved with this choice. The mass of the helicopter should not exceed 10kg. The goal of this study is to come up with a conceptual design program that determines the performance and weight decomposition of the final helicopter with equipment (masses) and size requirements as input variables. This conceptual design program will be the initial step before time consuming simulations using Computational Fluid Dynamics.

1.4 Experiment

In order to validate the use of the theories used in the conceptual design program, an experimental set-up is build. The first experiment is to check the correct working of the set-up, by repeating an experiment performed by Okochi et al. [12]. The second experiment is to check the validity of the proposed theory for single rotor using two different airfoils (flat plate & thin angular). The third experiment is to find the influence of the Mach number on the thrust and power coefficient. With this information, the conceptual design program can be updated with a Mach number correction. The final goal is to design a coaxial rotor and so the wake interference effect of the upper rotor on the lower rotor will be analyzed using a coaxial experimental set-up. With the same set-up, also the pitch difference between upper and lower rotor will be computed that assures torque balance between both rotors.

Chapter 2
Conceptual design program

The main idea behind the conceptual design program is to make a program that computes the performance, size and weight of the final helicopter in a simple but accurate way. For the computation of the thrust and power of the conceptual design program, the Blade Element Momentum Theory is applied. This theory is used as a simple but accurate tool at first stages of the design of free flow rotating blades (wind turbines, propellers and helicopters).

2.1 Blade Element Momentum Theory

For helicopters, this theory was introduced by Gessow et al. [13]. The theory divides the helicopter blade into a finite number of sections along the radial direction (dr) and applies momentum theory at each of these sections. With this method, a solution for the induced axial velocity distribution can be obtained. It is out of scope of this work to handle and derive this theory in detail for the application of a helicopter, details can be found in the paper by Gessow et al. [13]. The most important assumption of the theory is steady flow, it does not assume any turbulence. The theory is a pure 2D theory, which implies it does not account for more complex 3D effects such as swirl, tip losses, wake interference and rotational effects. However, the 3D effects can be accounted for by using empirical correction models.

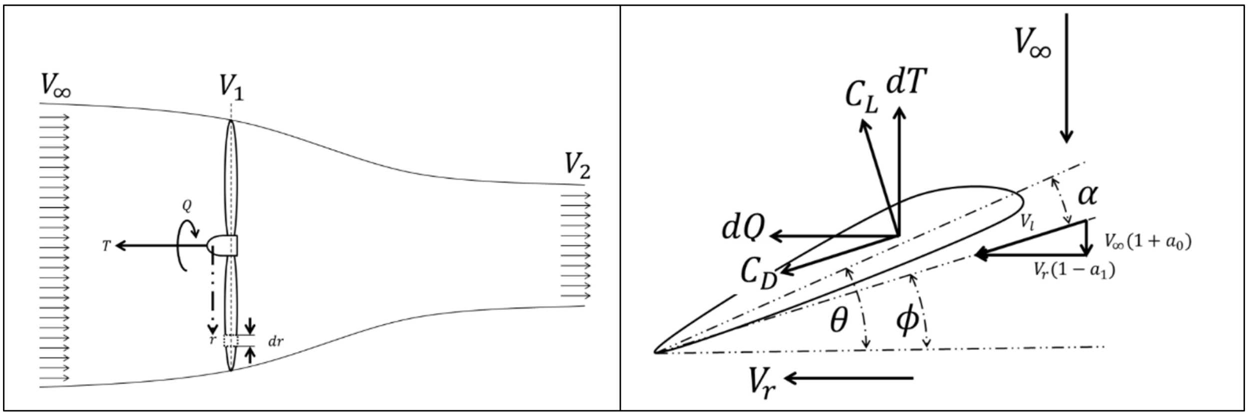

Figure 2.1: Blade Element Momentum Theory

2.1.1 Swirl

Besides giving axial thrust, the rotation of the blades also gives the wake a rotational swirl. This can be accounted for by adding a swirl velocity, proposed by Nikolsky et al. [14]. Following this model, it becomes clear that the swirl velocity is only significant close to the root. Because in general this part of the rotor does not produce significant thrust, the effect of taking swirl into account is negligible. On top of this, the proposed mission uses a coaxial rotor configuration. This implies that there will be (to some extent) swirl recovery caused by the counter-rotating set of rotor blades [15]. Therefore, the effect of swirl is not taken into account in the conceptual design.

2.1.2 Tip losses

The formation of a vortex at the tip of each blade produces a local high inflow ratio which will result in a reduction of the generated lift at the tips. Prandtl [16] provided a solution by simplifying the helical vortex sheets of the rotor wake by a series of 2D vortex sheets. With this model, a new axial velocity distribution can be found by adding a tip loss factor $F(r)$ that is dependent on the spanwise position r. Since the tip loss factor $F(r)$ is depending on the axial velocity distribution $\lambda(r)$, an iterative scheme needs to be used to compute $F(r)$ and the final velocity distribution. In Section 2.3, there is more information on how this is implemented in the design.

2.1.3 Wake interference coaxial rotor

As already described in the introduction, the helicopter will be a coaxial rotor configuration. This implies the bottom rotor will work in the wake of the upper rotor which will lead to a higher induced power coefficient of the lower rotor. The ratio between coaxial induced power coefficient and single rotor induced power coefficient can be computed using the momentum theory. However, it was proven that this way of accounting is overly pessimistic when compared with experiments [17]. This is caused by the complex flow phenomena that cannot be captured by the momentum theory. Therefore, in practice an interference factor is generally taken from experiments. As an initial starting point, the interference factor of coaxial rotor experiments performed by Harrington et al. ($\kappa_{int} = 1.16$) [18] is used and this factor will be validated by experiments (i.e. by comparing single rotor to coaxial rotor power consumption for different width between rotor disks).

2.1.4 Rotational effects

Rotating blade airfoils experience higher maximum lift coefficients compared to the maximum 2D airfoil lift coefficients. This stall delay is caused by a radial flow component which will thinner the boundary layer and will result in a delay of stall. This effect can be taken into account in the Blade Element Momentum Theory by means of a semi-empirical relation that modifies the local lift coefficient based on its angle of attack and proximity to other blade regions. The correction model used in this conceptual design program is proposed by Snel et al. [19]. This work showed good agreements with experiments and is used a lot in practical applications as correction model. The semi-empirical relation is given by the following Equation:

$$C_{L_{3D}} = C_{L_{2D}} + 3.1(c/r)^2(C_{L_{pot}} - C_{L_{2D}}) \tag{2.1}$$

In this Equation, the 2D lift coefficient comes from wind-tunnel data of the specific airfoil. The potential lift coefficient is defined as $2\pi sin(\alpha - \alpha_0)$. The factor 3.1 was used to fit with the experimental measurements. To match the extents of the 3D effects, this correction is applied between the root and 85% of the span, as was proposed by Snel et al.

2.2 Airfoil characteristics

Now that we have defined the theory used to analyze the performance of the helicopter, we need an airfoil shape that provide good performance at the low Reynolds regime the helicopter will fly ($\mathcal{O}(10^3) - \mathcal{O}(10^4)$). The forces on these blades are relatively small and therefore thinner airfoils compared to earth can be chosen. The references that are available for this are, by no coincidence, papers describing airfoils specifically for flight on Mars [10,20]. It has been shown by the references that the use of a sharp leading edge is favorable for flying in this Reynolds regime to avoid laminar separation. Also, the addition of small camber is favorable for the aerodynamic performance. For this conceptual design, the 6%h/c angular airfoil is chosen [20]. The maximum camber of 6%h/c is located at 0.3c and the thickness is 1%t/c. This airfoil compromises high lift over drag as well as a lift slope that is relatively insensitive to the change of Reynolds number (for Reynolds numbers higher than 3 000). Besides this, a large amount of data is available for this airfoil because this airfoil is investigated internally at JAXA. The polar data for this airfoil at different Reynolds numbers are visualized in Figure 2.2. Besides having a low Reynolds number, the airfoil will also be subjected to a locally high Mach number (increasing linearly towards the tip). With higher Mach numbers, flow phenomena become active earlier or later which is why normally a correction model is used to correct the lift (and sometimes drag) coefficient at higher Mach numbers. For Reynolds number flows higher than 100 000, the lift correction model by Prandtl-Glauert [21] is used in practical applications. However, for low Reynolds number flows, this correction model is invalid, proven by Anyoji et al. [22]. He found out that for low Reynolds number flows, the separation point will be shifted back by an increasing Mach number. This effect is affecting the lift coefficient and especially in the situation of a blunt leading edge. For the airfoils examined with a sharp leading edge, the effect at moderate angles of attack (i.e. below 7degrees) is negligible. This is why at first no Mach number correction model is taken into account. However, the particular airfoil that has been proposed for the helicopter is not examined by Anyoji et al. In order to improve the conceptual design program in the future, the influence of the Mach number will be examined using an experiment. Besides looking at the Mach number effect, Anyoji et al. also did research on the influence of the specific heat ratio on the lift and drag coefficient. On Mars, the atmosphere consists largely out of CO_2 with a different specific heat ratio compared to N_2 on Earth. The influence of the different specific heat ratio turned out to be negligible.

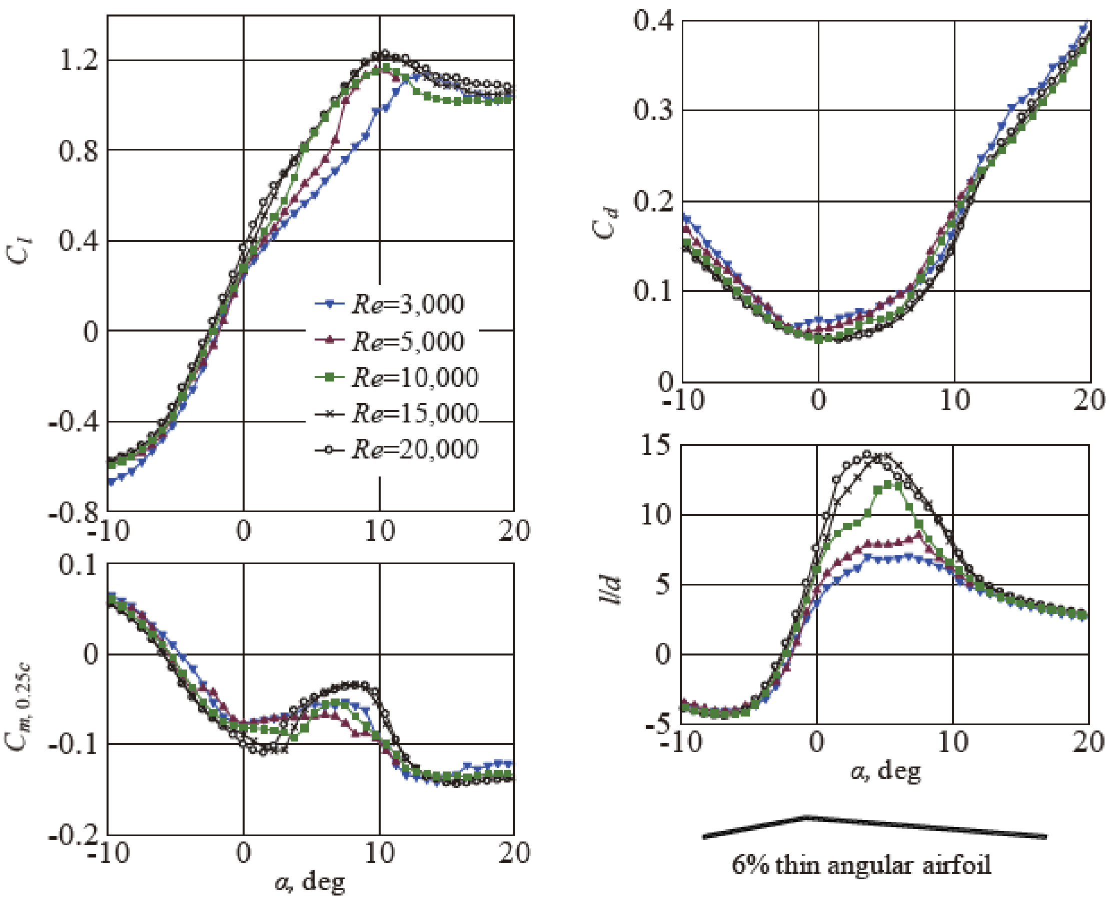

Figure 2.2: Airfoil polar data [20]

2.3 Design flowchart

Now the method for computing the inflow ratio and the airfoil data is known, a design flow chart is constructed that computes the dimensions and masses of the helicopter components, as well as the performance in terms of maximum flight time. This flowchart follows the procedure of conceptual helicopter design described by Leishman et al. [17]. The design flow chart is visualized in Figure 2.4. On the left, all input parameters are displayed. The values for these parameters are given in Appendix 1. An explanation of these input values is given in the paper of Aoki et al. [11]. On the right, the convergence loops are shown. For these four convergence loops, a stopping criteria of 1e-3 (difference between new and old computed value) is employed. The middle section of the flow chart are equations that are handled in the rest of this section. The flow chart starts with an initial total mass. With this initial total mass, the required thrust is obtained using Equation 2.2.

$$T_{req} = k m_{tot} g \tag{2.2}$$

In this Equation, the thrust margin k ensures that the helicopter also can move forward and has the ability to climb vertically. The thrust is computed using Equation 2.3 to 2.7. The Equation for computing the axial inflow ratio (Equation 2.4) follows from the Blade Element Momentum Theory. The derivation of this Equation is described by Leishman et al. [17]. In this expression, airfoil data (α_0 & $C_{L\alpha}$) is necessary. For this, airfoil data is fitted as a linear line with a zero lift angle of attack (α_0) and a lift slope ($C_{L\alpha}$). This has been done for several Reynolds numbers since the Reynolds number differs in spanwise direction. Also, the Prandtl tip loss factor F(r) is taken into account in Equation 2.4. To find this tip loss factor, the iteration scheme displayed in Figure 2.3 is used. The chord length is adjusted collectively over the complete span of the blades in order to obtain the required thrust computed in Equation 2.2.

$$\sigma = \frac{N_{blade} R (1 - r_{hub}) c}{N_{disk} \pi R^2} \tag{2.3}$$

$$\lambda(r) = \frac{\sigma C_{L\alpha}(Re)}{16F(r)} \Big(\sqrt{1 + \frac{32F(r)(\theta - \alpha_0(Re))r}{\sigma C_{L\alpha}(Re)}} - 1 \Big) \tag{2.4}$$

$$C_T = 4 \int_{r_{hub}}^{1} F(r) \lambda(r)^2 r dr \tag{2.5}$$

$$\omega = \frac{M_{tip} V_{sos}}{R} \tag{2.6}$$

$$T = C_T \rho N_{disk} \pi R^2 (\omega R)^2 \tag{2.7}$$

When the thrust is obtained, the final inflow ratio ($\lambda(r)$) is used again to compute the induced power coefficient using Equation 2.8. For this induced power coefficient, we also need the wake interference factor for the coaxial rotor configurations supplied by Harrington [18]. Furthermore, the angle of attack is computed in Equation 2.9 and with the quadratic fit of the drag coefficient depending on the Reynolds number, the profile power coefficient is computed in Equation 2.11. The total power coefficient is an addition of the profile power coefficient and induced power coefficient.

From this, the torque of the rotor while hovering is computed in Equation 2.13.

$$C_{p_{ind}} = 4\kappa_{int} \int_{r_{hub}}^{1} F(r)\lambda(r)^3 r dr \tag{2.8}$$

$$\alpha(r) = \theta - \frac{\lambda(r)}{r} \tag{2.9}$$

$$C_d(r) = C_{d_0(Re)} + d_1(Re)\alpha(r) + d_2(Re)\alpha(r)^2 \tag{2.10}$$

$$C_{p_0} = \int_{r_{hub}}^{1} \sigma C_d(r) r^3 dr \tag{2.11}$$

$$C_{p_{tot}} = C_{p_{ind}} + C_{p_0} \tag{2.12}$$

$$Q = N_{disk} C_{p_{tot}} \rho \pi \omega^2 R^5 \tag{2.13}$$

Now the chord distribution and power consumption is known, all masses are computed using Equation 2.14 to 2.19. If the total mass differs from the initial total mass more than the stopping criteria, the loop will be done over until convergence is reached. Also, the performance of the helicopter in terms of the total flight time is computed in Equation 2.22.

$$m_{rotor} = tc^2(1 - r_{hub}) R N_{blade} \rho_{rotor} \tag{2.14}$$

$$m_{motor} = \frac{P_{prop}}{\rho_{motor}} \tag{2.15}$$

$$m_{cable} = r_{cable} m_{tot} \tag{2.16}$$

$$m_{margin} = r_{margin} m_{equipment} \tag{2.17}$$

$$m_{hub} = N_{disk} \rho_{hub} \pi (r_{hub} R)^2 t_{hub} \tag{2.18}$$

$$m_{tot} = m_{rotor} + m_{motor} + m_{cable} + m_{equipment} + m_{frame} + m_{margin} + m_{battery} + m_{hub} \tag{2.19}$$

$$P_{prop} = \frac{1}{\eta} \omega Q \tag{2.20}$$

$$P_{tot} = P_{prop} + P_{equipment} \tag{2.21}$$

$$t_{flight} = \frac{m_{bat} \rho_{bat}}{r_{bat} P_{tot}} \tag{2.22}$$

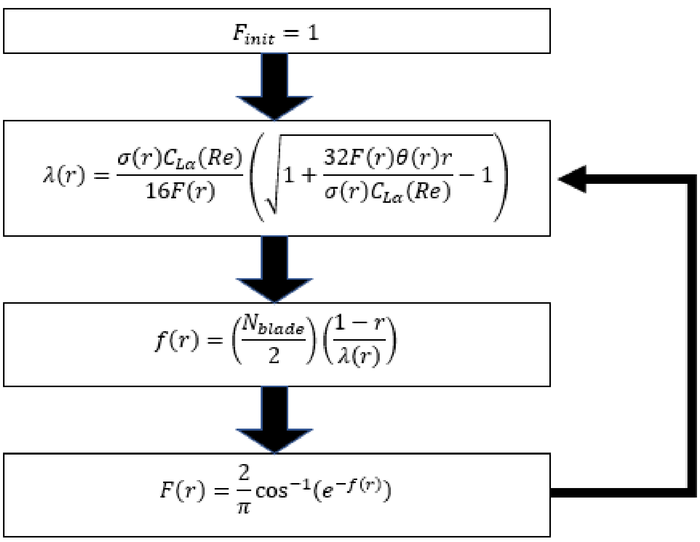

Figure 2.3: Prandtl tip losses iteration scheme

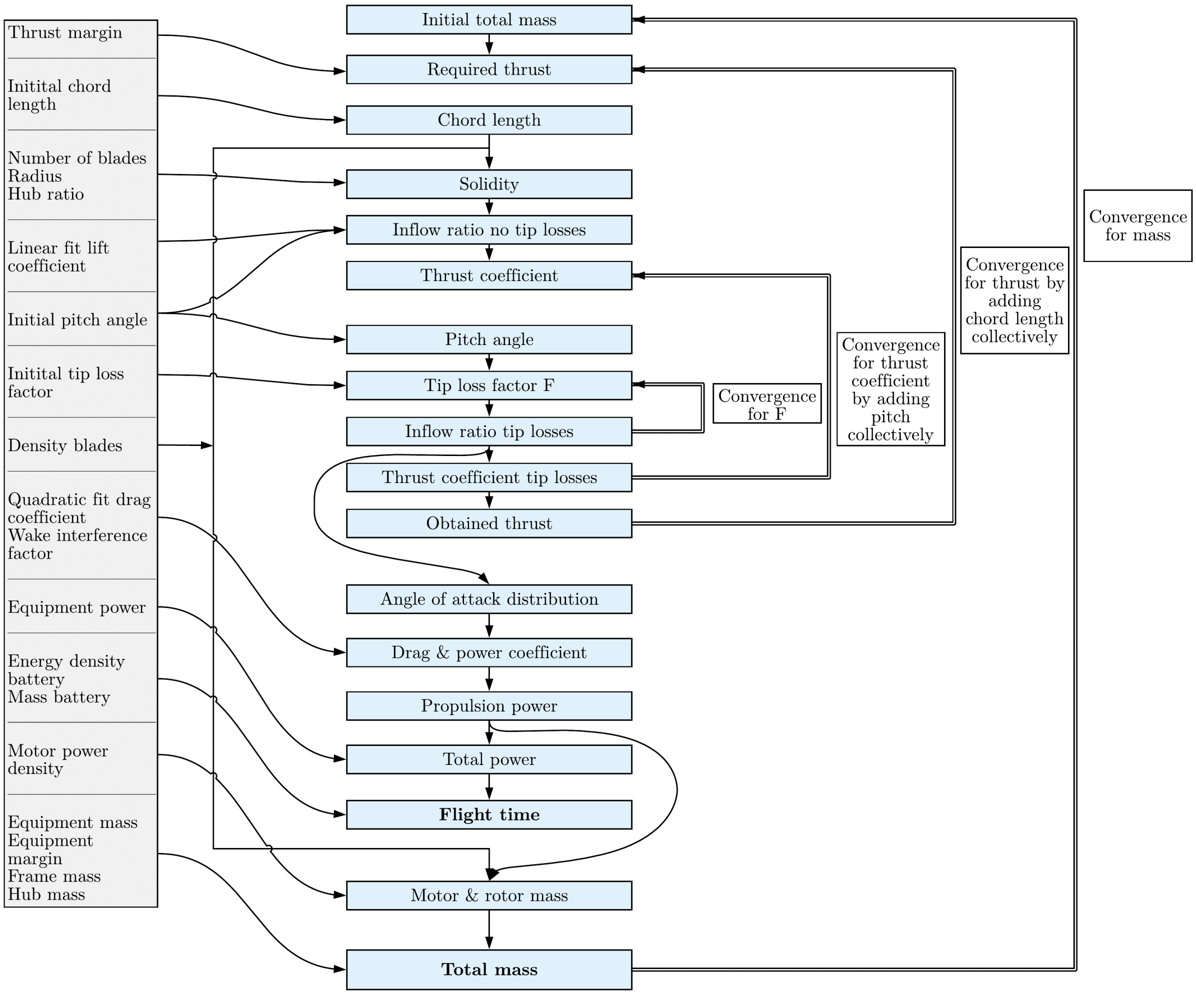

Figure 2.4: Conceptual design program flowchart

2.4 Addition of twist & taper

So far, we have limited ourselves to finding a helicopter blade with a rectangular planform shape and one collective pitch angle. By adding twist & taper, we search for a rotor planform that yields a longer flight time.

2.4.1 Ideal twist & ideal taper

The ideal rotor is the rotor that consumes both the lowest induced power as well as the lowest profile power. Since most of the time the helicopter will spend on hovering or slow forward flight, we limit ourselves in finding the ideal hovering rotor. The induced power can be minimized by requiring a uniform radial inflow and the profile power can be minimized by operating each section under their optimal angle of attack (i.e. angle of attack with highest L/D), depending on the airfoil used. According to the Blade Element Momentum Theory, the thrust coefficient of a rotor is defined as [17]:

$$dC_T = 4\lambda(r)^2 r dr \tag{2.23}$$

Also, the thrust coefficient can be written as the lift produced by the blades made nondimensional:

$$dC_T = \frac{N_{blade} dL}{\rho N_{disk}(\pi R^2)(\omega R)^2} = \frac{N_{blade}(\frac{1}{2}\rho V^2 c C_L dy)}{\rho N_{disk}(\pi R^2)(\omega R)^2} = \frac{1}{2}\Big(\frac{N_{blade} cR}{N_{disk}\pi R^2}\Big) C_L \Big(\frac{y}{R}\Big)^2 d\Big(\frac{y}{R}\Big) = \frac{1}{2}\sigma(r) C_L r^2 dr \tag{2.24}$$

If we substitute Equation 2.23 into 2.24 and solve for the inflow ratio $\lambda(r)$, we obtain Equation 2.25. We require now that all sections are working under the optimal angle of attack.

$$\lambda(r) = \sqrt{\frac{\sigma(r) r C_{L\alpha}(\alpha_{opt} - \alpha_0)}{8}} \tag{2.25}$$

The minimum induced power coefficient is found when the inflow ratio is constant along the span. This can be achieved by demanding the solidity is proportional to the inverse of the radial coordinate r, i.e.:

$$\sigma(r) = \frac{\sigma_{tip}}{r} \tag{2.26}$$

The σ_{tip} in Equation 2.26 can then be found by substituting Equation 2.26 into 2.25 and solving the integral with boundaries 0 to 1. The resulting equations for the solidity and chord distribution become:

$$\sigma(r) = \frac{4C_T}{C_{L\alpha}(\alpha_{opt} - \alpha_0) r} \tag{2.27}$$

$$c(r) = \frac{\sigma(r) N_{disk} \pi R^2}{N_{blade} R} \tag{2.28}$$

The pitch distribution becomes:

$$\theta(r) = \alpha_{opt} + \frac{\lambda(r)}{r} = \alpha_{opt} + \sqrt{\frac{C_T}{2}}\Big(\frac{1}{r}\Big) \tag{2.29}$$

Looking at Equation 2.29, the pitch distribution at the ideal twist situation is also proportional to the inverse of the radial coordinate r. In order to compute the mass decomposition and performance of the helicopter, the same conceptual design flowchart displayed in Figure 2.4 is used.

2.4.2 Linear twist & linear taper

From the initial results of the ideal twist & taper situation, it was found that the flight time was lower compared to the no twist situation. This result is the consequence of the chord distribution which causes the rotor mass to increase. Because the rotor mass is significant in the situation of a Mars helicopter, there is a large influence of this. An increase in rotor mass leads to a higher total mass, which in turn leads to a higher total power and lower flight time.To solve this, a linear twist & taper is proposed. For this, the twist & taper distribution of the ideal situation is approximated by a straight line constrained by the ideal twist & ideal taper evaluated at r=0.95 and r=1. Again, the same flowchart is used.

2.4.3 Ideal twist & linear taper

Another possibility is to use the ideal twist distribution in combination with linear taper. The idea is that this situation describes the optimum angle of attack distribution fairly well while still have low rotor mass by applying linear taper. Again, to obtain convergence of thrust, the pitch angle is added collectively. Again, the same flowchart is used.

2.5 Results

In this section, the results of the conceptual design program are handled. For this, the influence of changing the input parameters has been examined. As a result, the best performing helicopter in terms of maximum flight time has been investigated in more detail.

2.5.1 Effect of pitch angle

For the case of no twist and taper, the collective pitch angle is the variable that determines the aerodynamic performance. In Figure 2.5, the angle of attack distribution is visualized over the span for pitch angles varying from 10 degrees up to 25 degrees. Higher than 15 degrees pitch angle results in the angle of attack near the tip approximating 10 degrees. Looking at the 2D airfoil data, an angle of attack exceeding 10 degrees will result in stall. The 3D lift corrected stall delay is not applicable in this tip region. Stall implies that the linear fit of the lift coefficient is invalid, which makes the results of thrust and power for pitch angles higher than 15 degrees invalid. Also, stall is something that we want to avoid because of its unsteady behaviour.

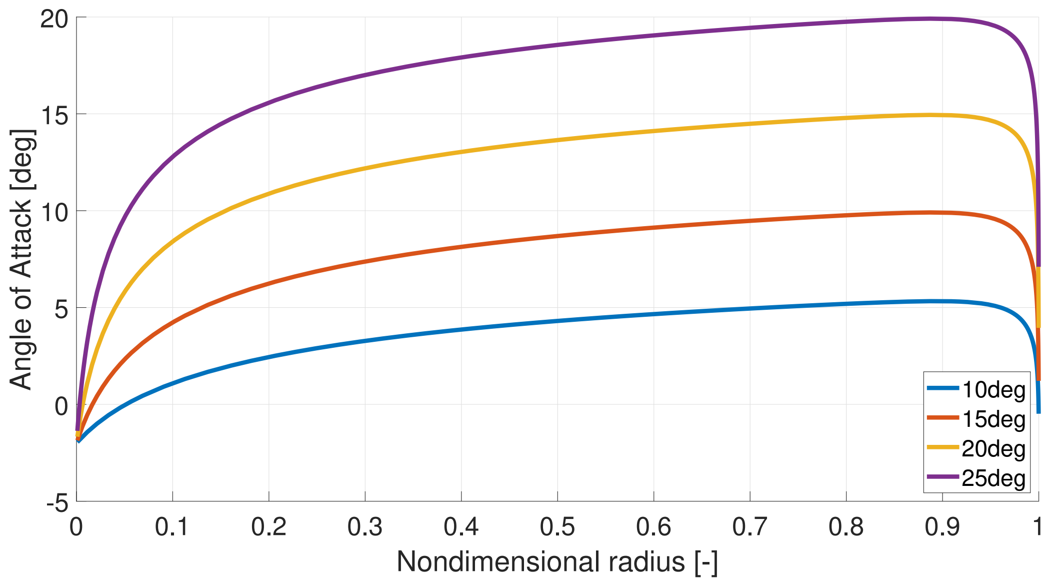

Figure 2.5: Angle of Attack for different collective pitch angles

The pitch angle is now varied from 10 to 15 degrees in steps of 1 degrees, and the battery mass is varied to simulate the effect of different thrust (coefficients). The total mass versus flight time is visualized in Figure 2.6. As can be seen from this Figure, a lower pitch angle is favorable for low mass, and thus low thrust coefficient. This is because at these lower pitch angles, the optimum angle of attack of about 5 degrees (highest lift over drag) is matched very well. At higher mass (and thus higher thrust coefficient), the effect of increasing rotor mass plays a role which results in a higher power coefficient and thus reducing the flight time. Looking at Figure 2.6, 12 degrees pitch angle turns out to be the best choice regarding flight time over the whole mass range.

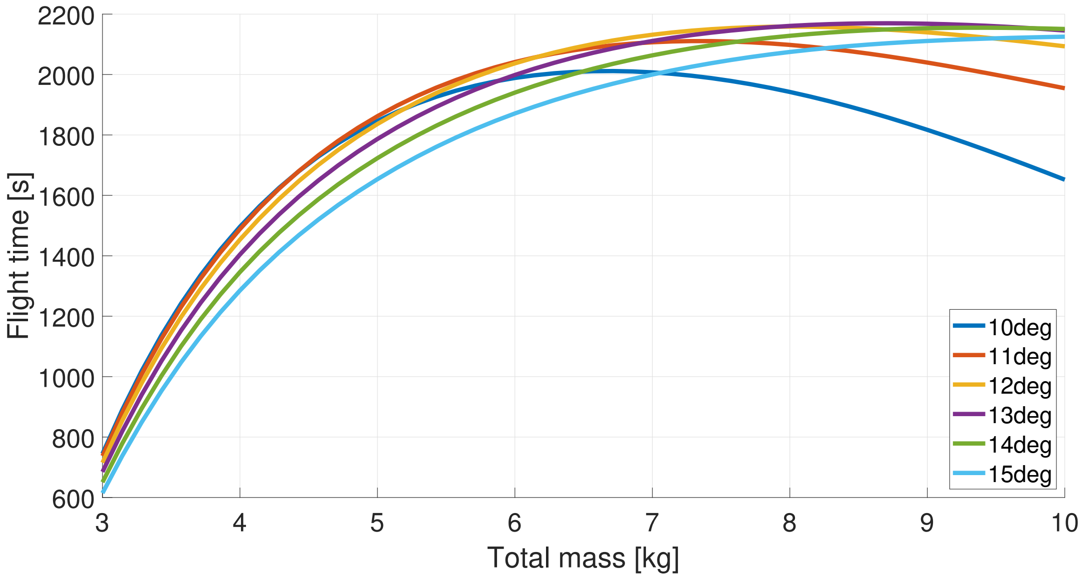

Figure 2.6: Flight time versus total mass for varying pitch angles

2.5.2 Effect of twist & taper

To see the effect of twist and taper, the flight time versus total mass graph is displayed in Figure 2.7. For the no twist situation, the pitch angle of 12 degrees is chosen. As can be noticed, the ideal twist situation clearly has lower flight time. The reason for this result is the high rotor mass, compared to the linear taper and no taper situation. The ideal twist with linear taper combination yields the highest flight time. At about 8kg total mass, there is an optimum for the flight time.

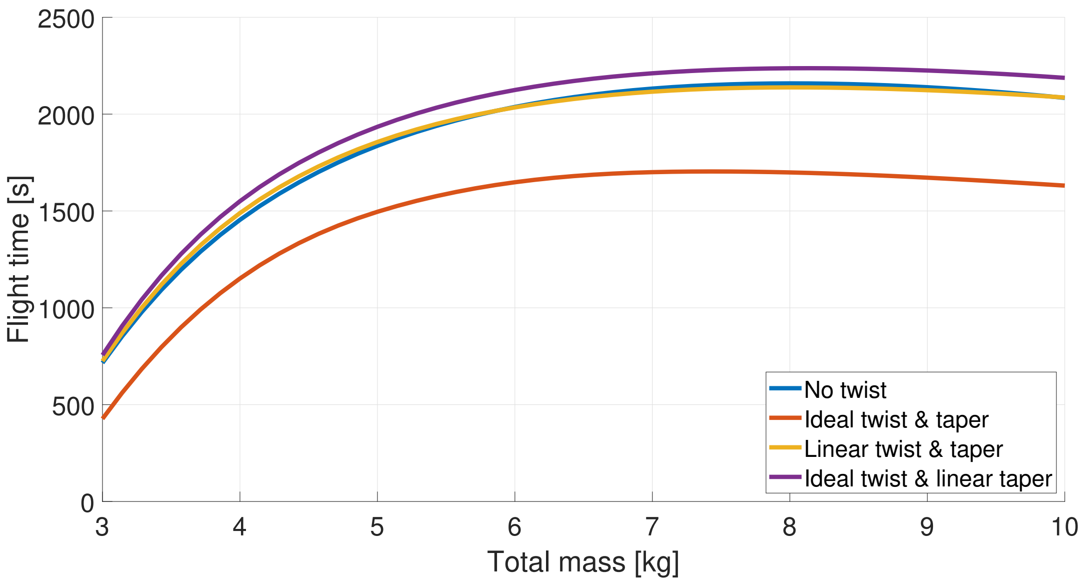

Figure 2.7: Flight time versus total mass for varying planform choice

2.5.3 Effect of rotor radius

Up to now, all cases had a fixed radius of 1m. Structural and/or size requirements can cause this radius to change. To see this effect, the radius is made variable from 0.6m up to 1.2m with step size of 0.2m. The ideal twist with linear taper is applied as planform shape since it yields the best performance. Again, the total flight time is plotted against the total mass in Figure 2.8. As expected, the higher the rotor radius the higher the maximum flight time. Also, the total mass at maximum flight time increases by increasing rotor radius.

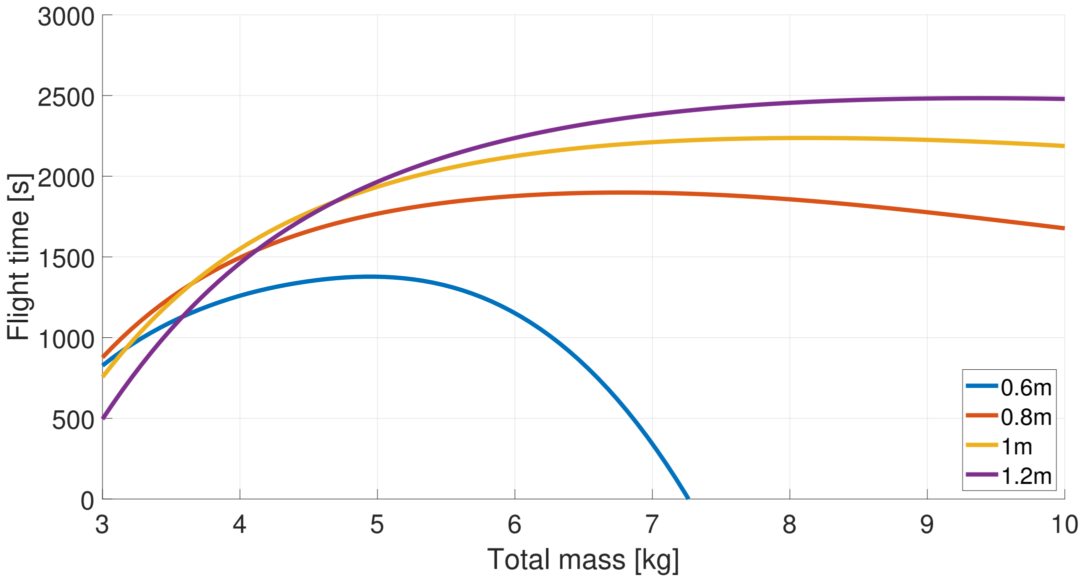

Figure 2.8: Flight time for varying radius

2.5.4 Specifications maximum flight time helicopter

From Figure 2.7, the maximum flight time is achieved with the ideal twist and linear taper planform. Figure 6.2 shows the pitch and resulting angle of attack distribution of the maximum flight time situation. As can be seen, the angle of attack distribution exceeds the 2D stall angle close to the root. However, while taking into account the 3D stall delay correction model, this would not cause any problems. Furthermore, in commercial helicopters it is conventional to limit the pitch angle close to the root to a certain maximum. In this case, limiting the maximum pitch to 25 degrees would be a good solution. Because the root does not produce high thrust and consume high power, this will only influence the performance marginally. Figure 2.10 show the chord distribution in the maximum flight situation. Figure 2.11 show the Reynolds number distribution. Table 2.1 and 2.2 show specifications and mass decomposition of the maximum flight time situation, respectively. Note that the hovering efficiency (FoM) is computed with thrust and power coefficient from one disk which is conventional for coaxial rotors. As can be seen in Table 2.2, the battery mass is about half of the total mass. An artist' rendering of the proposed Mars helicopter is shown in Figure 2.12.

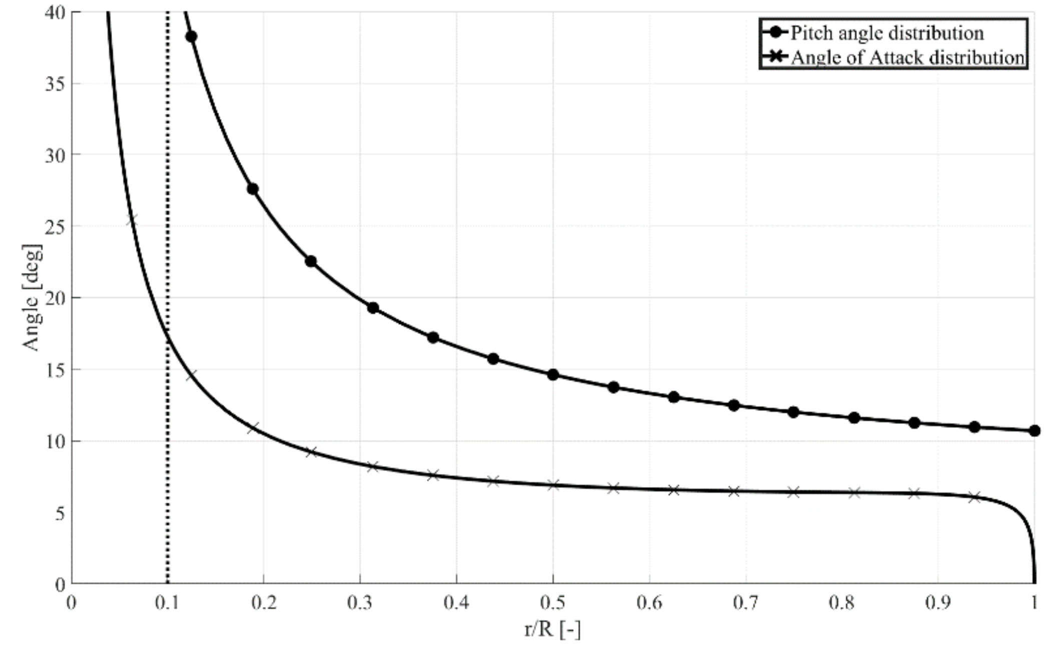

Figure 2.9: Pitch angle and resulting Angle of Attack distribution

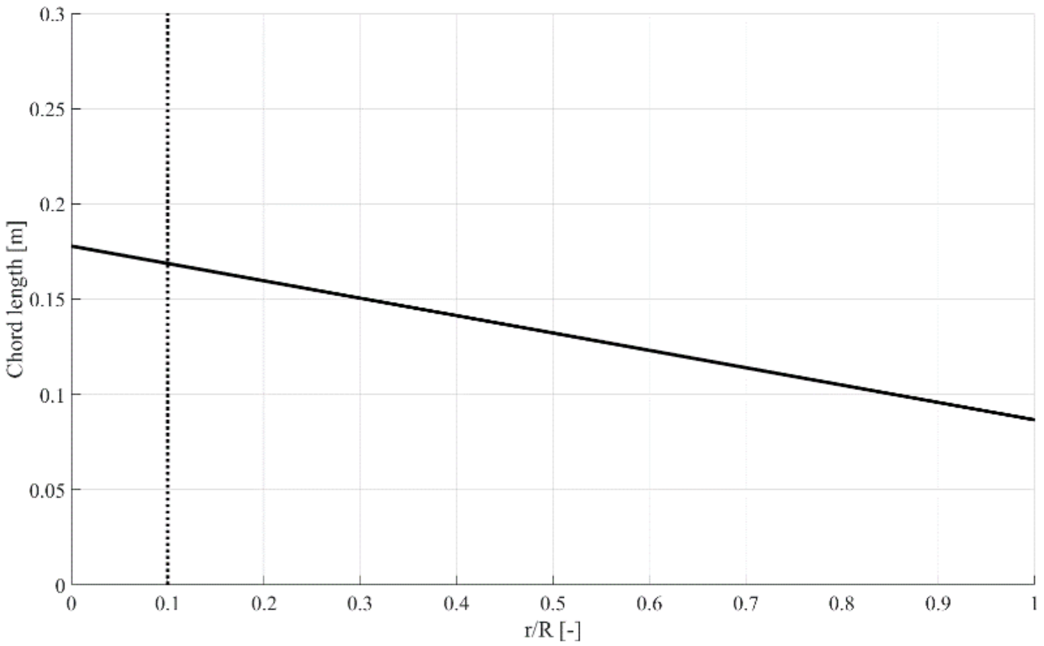

Figure 2.10: Chord length distribution

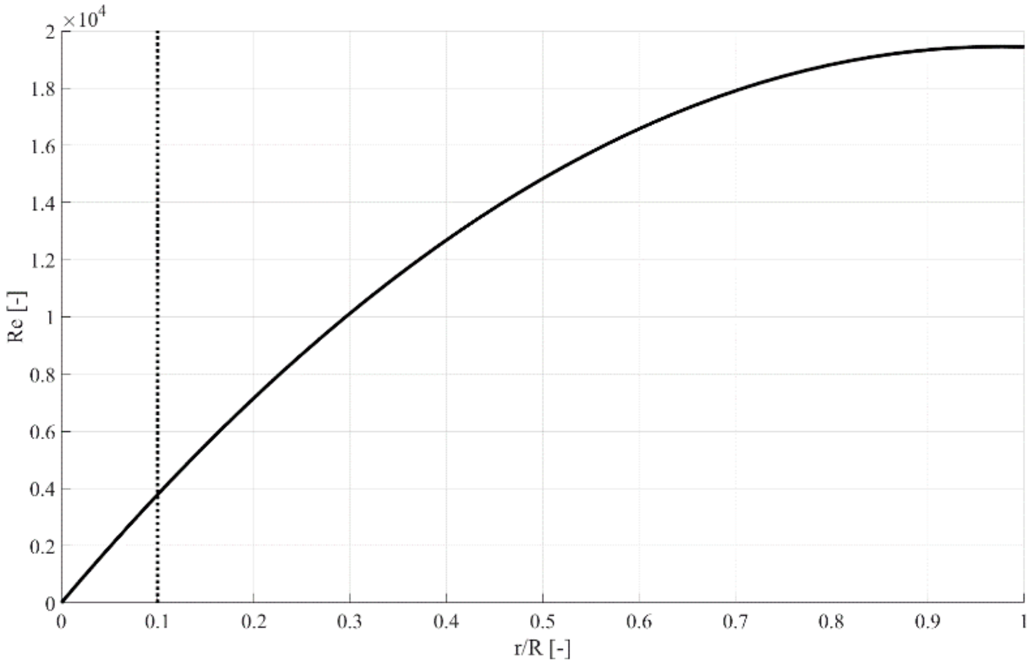

Figure 2.11: Reynolds number distribution

Table 2.1: Final specifications

Total mass [kg]	7.83
Time flight [s]	2235
Rotor radius [m]	1
Aspect ratio [-]	9.35
Rotational speed [rpm]	1681
Thrust coefficient [-]	0.0184
Power coefficient [-]	0.00292
FoM [-]	0.427

Table 2.2: Mass decomposition

	Mass [kg]	Percent [%]
Equipment	1.03	13
Motor	0.56	7
Rotor	0.95	12
Hub	0.47	6
Battery	3.92	50
Structure	0.36	5
Cable	0.23	3
Margin	0.31	4
Total	7.83	100

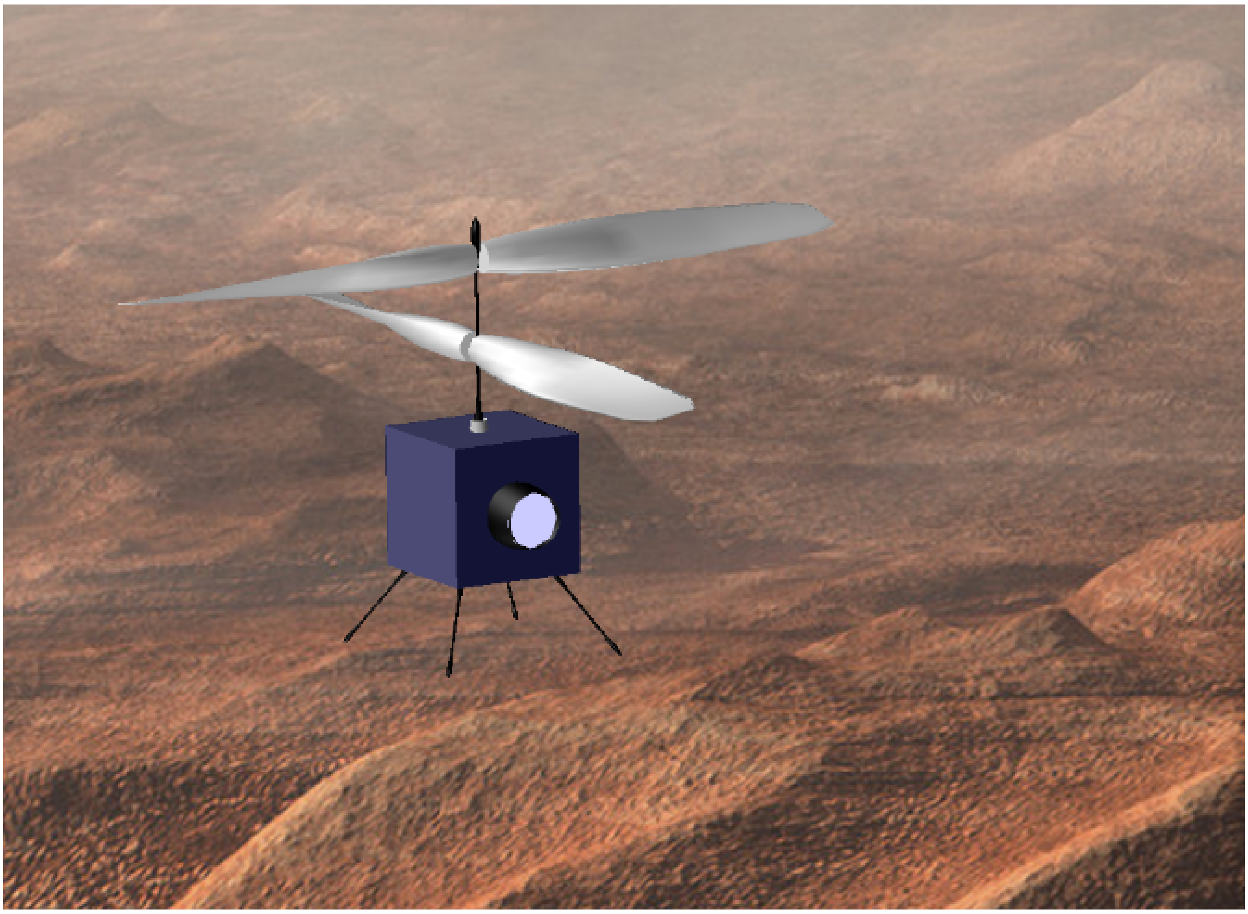

Figure 2.12: Artist's rendering of Mars helicopter [11]

Chapter 3

Experimental validation

In order to validate the use of the Blade Element Momentum Theory in the flight regime, experiments have been performed. The helicopter will fly in a Reynolds Mach number combination that is rarely seen on earth, i.e. Re $\mathcal{O}(10^3) - \mathcal{O}(10^4)$ combined with a tip Mach number approaching transonic flow (i.e. $M_{tip} = 0.8$). To simulate a helicopter flying in this regime, hovering experiments are performed in a vacuum tank. The pressure and rotational speed is adjusted to match the Reynolds and Mach numbers.

3.1 Experimental set-up

The hovering test stand used in the experiment is shown in Figure 3.1. In Figure 3.2, a schematic overview of the test stand is displayed with its most important components. The thrust of the blades is measured indirectly by measuring the shaft angle (α). The set-up works as an inverse pendulum. The reason for using an inverse pendulum is that with this method, low thrust values can be measured accurately by changing the support position of the shaft (i.e. by changing L_{pivot} with respect to L_{cg}) and by changing the mass of the counterweight. With a small thrust of the blades, a large angle difference can be noticed. The two sets of blades turn in opposite direction but with the same rotational speed. In Appendix 2, two more images are displayed with the test stand installed inside the vacuum tank. Within the vacuum tank, the metal underplate seen in Figure 3.1 is supported by three plastic leveling feet in order to reduce vibrations and to level the set-up.

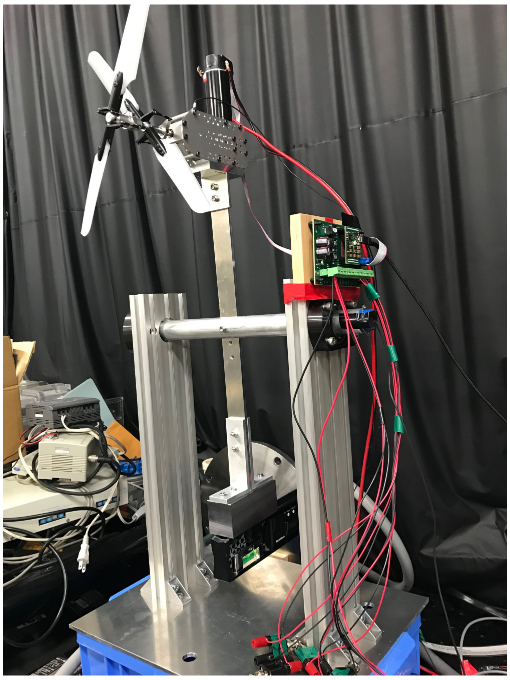

Figure 3.1: Pendulum test stand

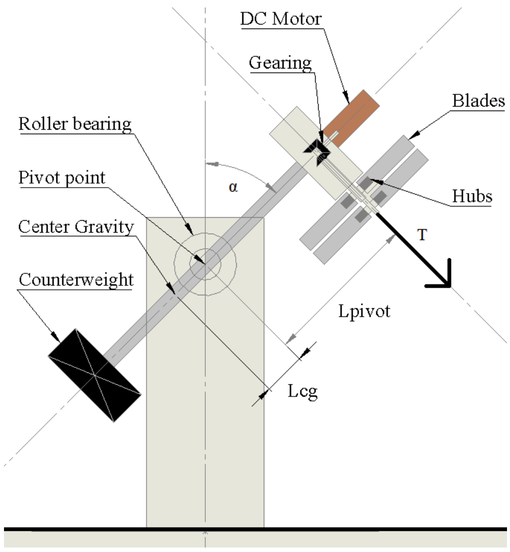

Figure 3.2: Schematic overview pendulum test stand

The thrust follows from a linear relationship with the shaft angle. The thrust coming from the blades is equal to:

$$T = C_{thrust}(\alpha_{rotation} - \alpha_{no-rotation}) \tag{3.1}$$

The way this thrust constant (C_{thrust}, not to confuse with thrust coefficient C_T) is computed will be discussed in Section 3.2.2. The thrust coefficient is the thrust made non-dimensional, i.e.:

$$C_T = \frac{T}{\rho(\omega R)^2(\pi R)^2} \tag{3.2}$$

The density ρ is computed using the ideal gas law (Equation 3.3). The pressure in the vacuum tank is measured independently at three positions. The temperature is measured independently at two positions using a T-type thermocouple.

$$\rho = \frac{P}{RT} \tag{3.3}$$

The motor used in the experiment is a DC motor. A characteristic of a DC motor is that the torque has a linear relationship with the supplied current. The constant that determines the slope of this relationship is called the torque constant. The torque coming from the blades is equal to:

$$Q = C_{torque}(I_{blade} - I_{no-blade}) \tag{3.4}$$

The way this torque constant (C_{torque}, not to confuse with torque coefficient C_Q) is computed will be discussed in Section 3.2.4. The reason we take the no blade current into account is because this current arises from friction of the gears and internal motor friction and we only consider the torque coming from the blades. The torque coefficient is the torque made non-dimensional, i.e.:

$$C_Q = \frac{Q}{\rho(\omega R)^3(\pi R)^2} \tag{3.5}$$

3.2 Component verification

Before starting the experiments, the functioning of the individual components need to be verified and the thrust and torque constant need to be determined.

3.2.1 Inclinometer

The inclinometer is used for measuring the pivot shaft angle. The inclinometer used is Seika NA3-30 [23]. This inclinometer is attached to the crosscut side of the shaft. The inclinometer gives a voltage which can be converted to an angle in degrees using Equation 3.6:

$$\alpha_{incl} = 15(V_{incl} - 2.5) \tag{3.6}$$

For verification of the inclinometer, a digital level was attached to the bottom of the counterweight. The angle of the digital level was compared to the measured value by the inclinometer for several cases. According to Figure 3.3, these data coincide well, which concludes a correct working of the inclinometer. The digital level itself has an accuracy of ± 0.05 degrees, which explains the small deviation between the two data series.

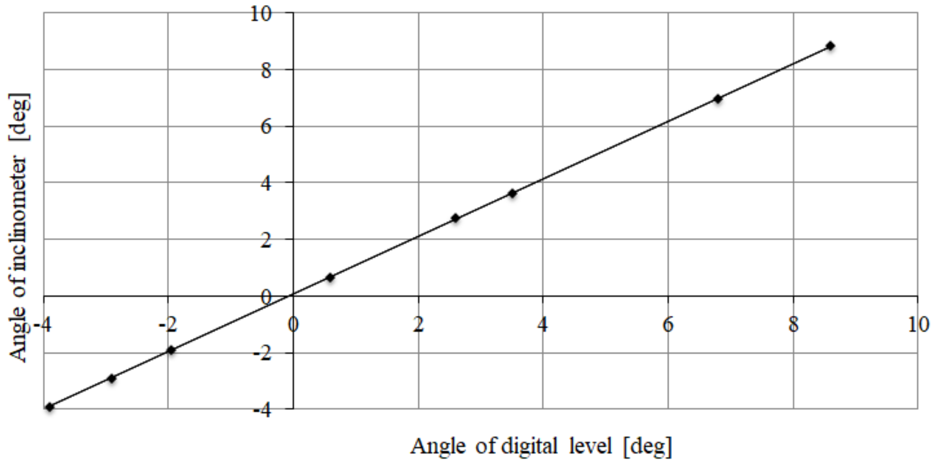

Figure 3.3: Inclinometer verification

3.2.2 Thrust constant

Now a relationship between the acquired thrust and the angle of the inclinometer need to be established. This relationship can be found analytically by considering the weight and mass center of each individual component. This is, however, very hard to perform and therefore the relationship is found experimentally. For this, a thread system has been applied. The thread is at one side attached to the gearing hub and on the other side attached to a counterweight. A schematic view of this set-up is displayed in Figure 3.5. Note that the blades are not rotating during this experiment. The weight of the weight is measured and by using geometry analysis and measuring the relevant dimensions, the thrust can is computed. At the same time, the inclinometer angle is measured. When different weights are used a relationship can be found between the thrust and the inclinometer angle. The relationship between the thrust and angle of the inclinometer can be seen in Figure 3.4. For a different set-up of support position, counterweight and blade weight, this experiment need to performed over since the thrust constant differs. For this specific set-up, the thrust constant is equal to $49.23N/deg$.

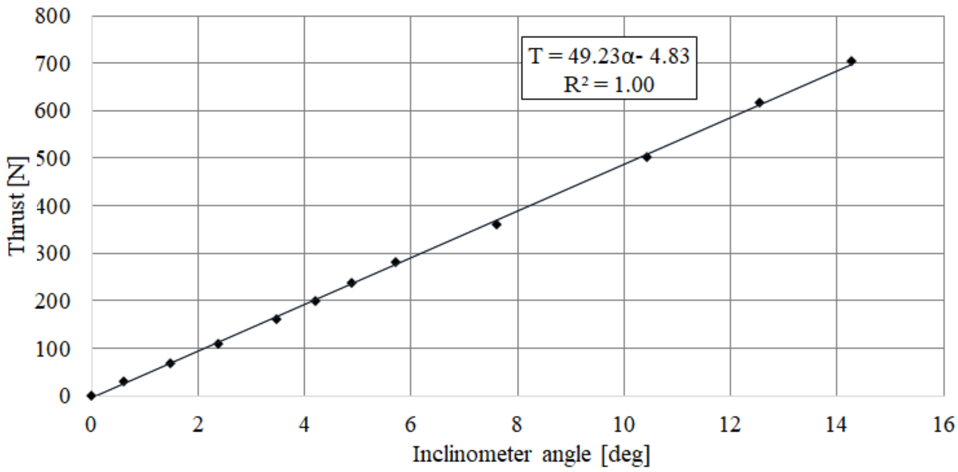

Figure 3.4: Relationship thrust and angle determination

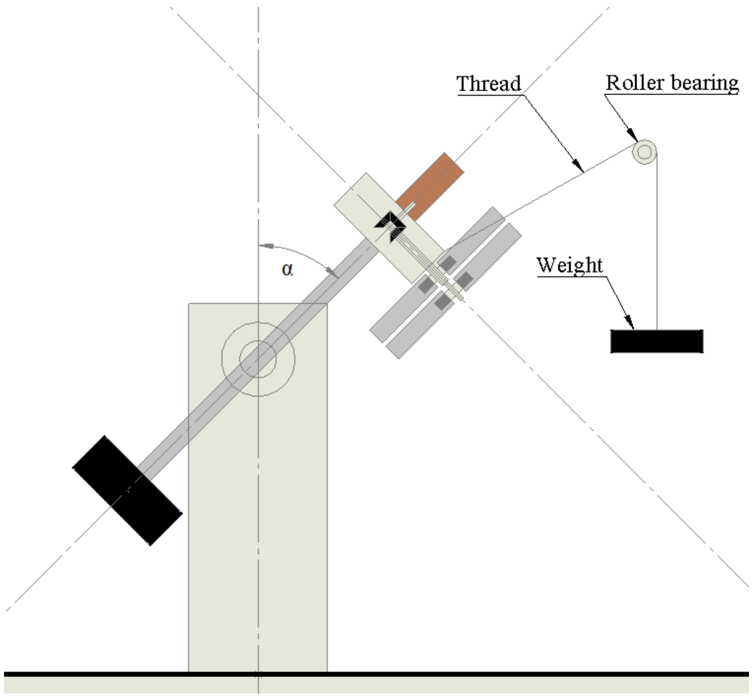

Figure 3.5: Schematic overview thread system

3.2.3 Rotary encoder

The rotary encoder is fixed to the motor and is used for measuring the rotational speed of the motor. The working of the rotary encoder is verified using a light source emitter and receiver. When the blade is passing, it blocks the light and therefore the voltage of the signal drops. The used emitter and receiver are Omron E3Z-T61 [24]. A sample frequency of 10 000Hz is used to effectively capture the passing of the blades. The rotary encoder is read by the supplied software of the motor controller (Escon studio 2.2 [25]). Consequently, the number of voltage drops is compared to the rotational speed of the encoder. According to Figure 3.6, these data coincide, which concludes a correct working of the rotary encoder.

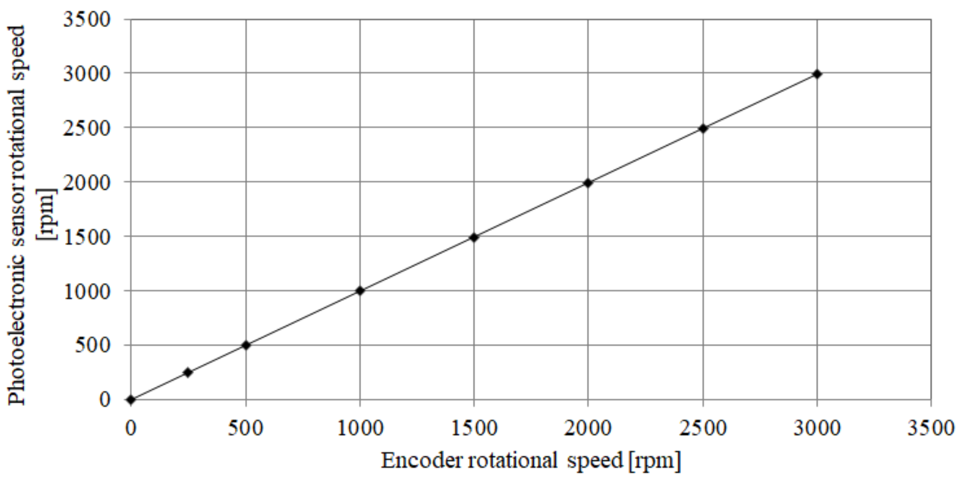

Figure 3.6: Encoder verification

3.2.4 Torque constant

According to the datasheet of the applied motor (Maxon RE35 part number 273753), this torque constant is 38.9[mNm/A] [26]. However, this value can differ from motor per motor because of production variations and therefore it is a standard procedure to check this constant. The constant is checked by attaching a weight to a small chord which is attached to a pulley. The pulley is fixed to the motorshaft. When raising the counterweight at a constant speed, there is no angular acceleration of the weight so the moment is balanced. By measuring the weight of the counterweight and simultaneously measure the current running through the motor, the torque generated can be computed. With this, the torque constant can be computed experimentally and compared by the value listed in the datasheet. This method has been performed for several torque values and the result can be seen in Figure 3.7. The resulting torque constant is computed at 37.24[mNm/A], significantly lower than the value listed in the datasheet.

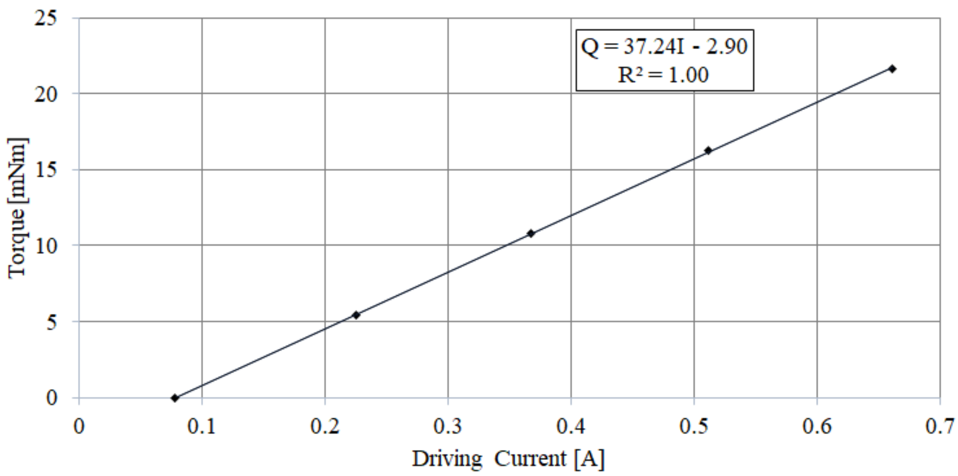

Figure 3.7: Torque constant determination

3.3 Validation experiment

In order to verify the correct working of the complete set-up, one case of the experiment performed by Okochi et al.[12] is repeated. He analyzed the performance of a single rotor by also using the same way of calculating the thrust, i.e. by using a pendulum. Okochi et al. analyzed the effect of the Aspect Ratio at different collective pitch angles at low Reynolds numbers. As a blade, he only considered a flat plate with 5%t/c. As validation experiment, the blade of Aspect Ratio is equal to 4 is chosen and for a pitch angle of 20 degrees, the thrust and power coefficient is computed under the same specified ambient pressures. In Table 3.1 the blade characteristics for this experiments are displayed. The blades are small enough to not cause any blockage & ground effect in the large vacuum tunnel. In Table 3.2, the differences between this experiment and the experiment performed by Okochi et al. are displayed. As can be seen in this Table, there is a small difference between the thrust coefficient computed by Okochi et al. and our measurements. This small difference can be explained by the fact that the hub ratio (hub length with respect to rotor radius) is slightly different for both experiments. The hub ratio is 0.165 and 0.227 for the experiment performed by Okochi and our experiment, respectively. Also, it is not listed by Okochi et al. what the ambient temperature was at the time of the measurement. This has an influence on the Reynolds number and so on the thrust coefficient. The power coefficient is similar for both situations which validates the correct working of the set-up.

Table 3.1: Blade characteristics validation experiment

Number of disks	1(single rotor)
Airfoil	Flat plate
Material	Plywood
Number of blades	2
Rotor radius	0.15[m]
Chord length	0.0316[m]
Speed	2400[rpm]
Hub ratio	0.165 (Okochi) & 0.227 (validation)

Table 3.2: Differences Okochi & validation experiment

Ambient pressure	C_T Okochi	C_T Validation	C_P Okochi	C_P Validation
10[kPa]	0.016	0.015	0.0058	0.00584

3.4 Reynolds number effect

Now, the Reynolds number effect will be examined for both the thrust and power coefficient. In this work, the flat plate of 1.3%t/c and thin angular airfoil of 6%h/c 1%t/c are analyzed in terms of thrust and power. The characteristics of the blades are displayed in Table 3.3. The blades are small enough to not cause any blockage & ground effect in the large vacuum tunnel. The airfoils used in the experiment have proven to be a high performance (high L/D) in the low Reynolds number range. With this 2D airfoil data[20], the theory of the Blade Element Momentum Theory that is used in the conceptual design program can be validated. In order to see the Reynolds number effect on the performance, the pressure is varied while keeping the rotational speed constant at 1000rpm. With this approach, the Mach number stays constantly low at 0.05. With this Mach number, no compressible effect is expected. Table 3.4 shows the measured pressures and corresponding tip Reynolds numbers in our set-up (where the Reynolds number is approximated value caused by small temperature & pressure fluctuations during the experiment):

Table 3.3: Blade characteristics

Number of disks	1(single rotor)
Airfoil	Flat plate & thin angular
Material	Steel sheet metal
Number of blades	2
Rotor radius	0.15[m]
Chord length	0.03[m]
Speed	1000[rpm]
Hub ratio	0.23[-]

Table 3.4: Ambient pressure and related Reynolds number

Ambient pressure [kPa]	10	16.5	33	49.5	66
Tip Reynolds number	3 000	5 000	10 000	15 000	20 000

The thrust coefficient is plotted against collective pitch angle for the flat airfoil and triangular airfoil, in Figure 3.8 and 3.9, respectively. If we compare both graphs, we can see that the Reynolds effect is larger using the triangular airfoil. This Reynolds effect can be explained by looking at the difference in 2D lift coefficient data, displayed in Figure 3.10. For the flat plate, large differences between the three Reynolds numbers considered is only visible at higher angle of attack. For the triangular airfoil, however, large differences are already present at lower angles of attack. Also, the thrust coefficient computed for the case of Re=20 000 using the Blade Element Momentum Theory using 2D airfoil data is shown in these graphs. Both show fairly good agreement up to pitch angles of 20 degrees. When looking into the angle of attack distribution at 20 degrees pitch angle, it was observed that the angle of attack exceeded 10 degrees at most of the blades. This leads, according to the 2D airfoil data, to stall which is not captured in the theory.

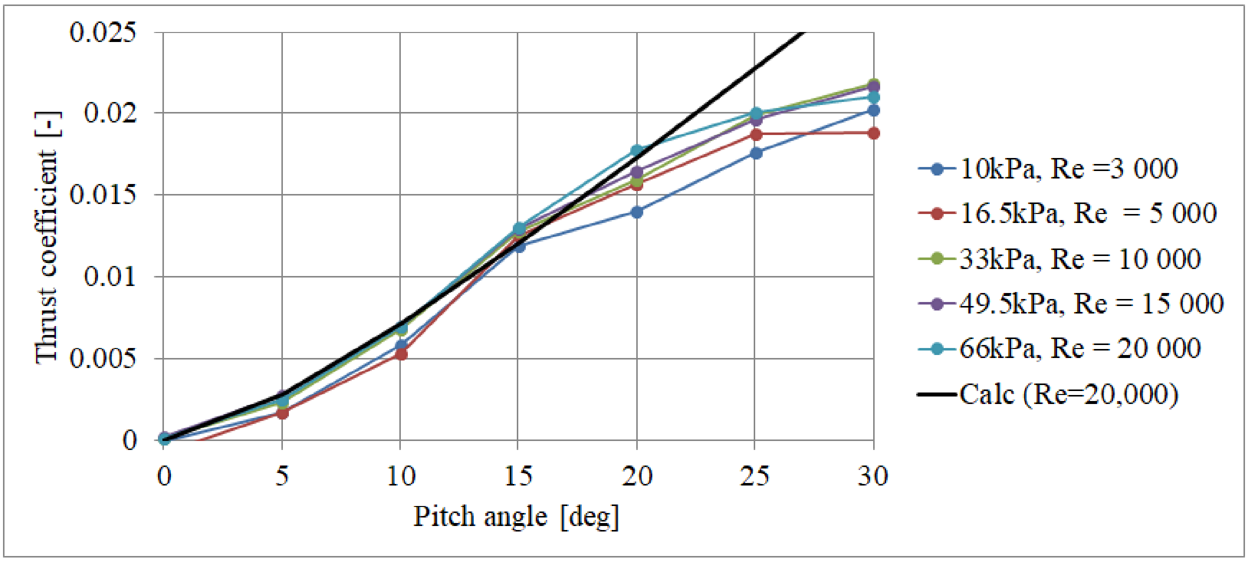

Figure 3.8: Thrust coefficient flat plate airfoil

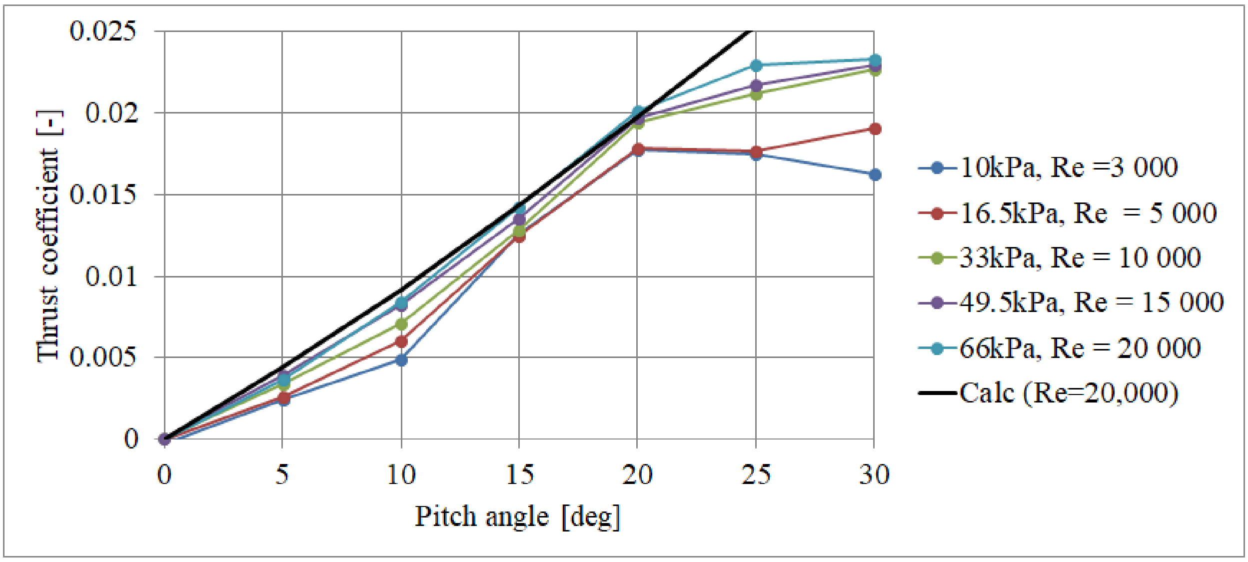

Figure 3.9: Thrust coefficient thin angular airfoil

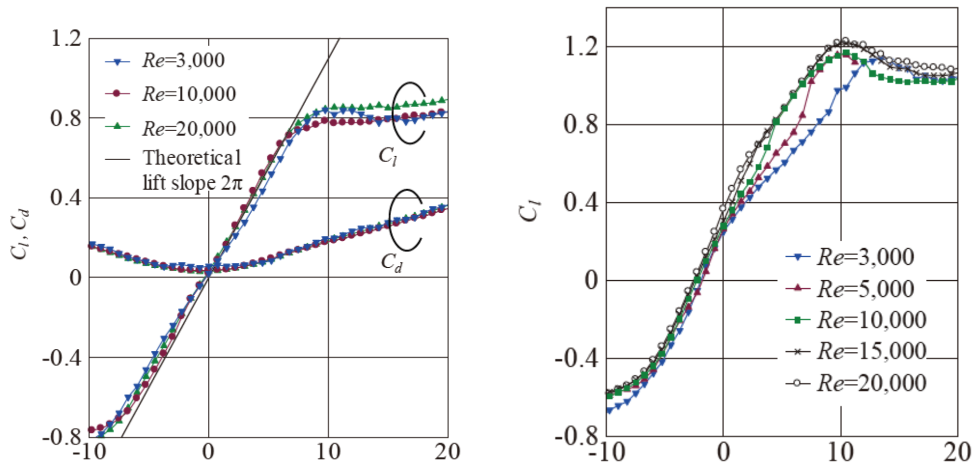

(a) Flat plate (b) Thin angular

Figure 3.10: Lift coefficient versus angle of attack [20]

In Figure 3.11, the power coefficient is visualized against the pitch angle for the thin angular airfoil. As can be seen, for a tip Reynolds number of 3 000 and 5 000, the power coefficient is significantly higher than the cases of 10 000, 15 000 and 20 000. Again, using the theory a line is plotted that visualizes the case of Re= 20 000. As can be seen, up to 20 degrees pitch angle, again there is good agreement between the used theory and the experiment. Unfortunately, we did not have enough time to finish the experiments of computing the power coefficient for the flat plate airfoil.

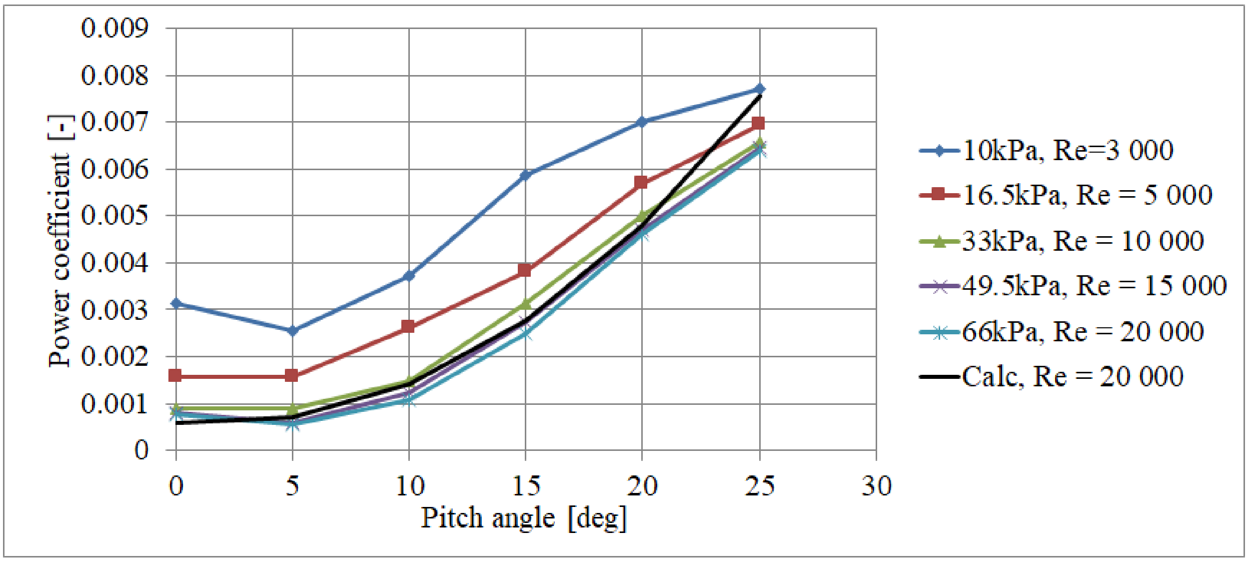

Figure 3.11: Power coefficient thin angular airfoil

3.5 Mach number effect

As already described in Section 2.2, the Mach number effect is initially not taken into account in the conceptual design program. However, the validity of this assumption will be tested using an experiment in the future. To see the Mach number effect on the helicopter performance, the rotational speed is made variable. With a changing rotational speed, the Reynolds number also changes. This can be be counteracted by changing the pressure at the same time. By matching the pressure change and rotational speed change, the Reynolds number can be kept constant while making the Mach number variable. The data at different tip Mach numbers can than be compared by the data at low tip Mach number (i.e. incompressible). With this result, the conceptual design program can be improved by making a correction factor for both the lift and drag coefficient at the combinations of Mach & Reynolds numbers considered.

3.6 Coaxial rotor - Width between rotor disks

As already described in Section 2.1.3, the wake interference factor of 1.16 has been taken from experiments performed by Harrington et al. [18]. It is expected that the wake interference factor has a relation with the width between the two rotor disks. Therefore, the width between the rotor disks will be varied to find this relation. The power will be computed using single rotor and coaxial rotor configuration. The ratio between these two configurations equals the wake interference factor.

3.7 Coaxial rotor - Torque balance

An advantage of using a coaxial rotor configuration is to not necessarily need a tail rotor. The torque of the upper and lower disks are than of the same magnitude but directed opposite to obtain torque balance. Since the lower disk is operating in the wake of the upper rotor, both rotors need to have different pitch to obtain this torque balance. This experiment will be performed in the future. In this experiment, the pitch of the upper rotor will be fixed and the lower rotor varied. A new set-up has to be build that is capable of computing the torque of the upper and lower rotor separately.

Chapter 4

Conclusion & future work

A mission for exploration of Mars' pit craters and caves using a helicopter is proposed by JAXA. Because of the atmospheric difference between Mars and the Earth, the aerodynamic design is the key factor in this complex design problem and is handled in this work. For this, a conceptual design program has been written that uses the Blade Element Momentum Theory to solve for the thrust & power. This theory is a simplified 2D model that is used for conceptual design in practical applications. The important 3D effects as wake interference for coaxial rotor, tip losses and rotational flow stall delay have been incorporated in this conceptual design program by using (semi-)empirical relations. A parametric analysis have been made that shows the relative influence of the input parameters on the total flight time. With a linear taper and ideal twist distribution, the helicopter has sufficiently long flight time to complete the missions successfully. With a radius of 1m, the total flight time is about 2235s. Also, the total mass is reasonably low at 7.83kg.

In order to validate the theory that has been used in the conceptual design program, a hovering stand is build and experiments are performed. Experiments are performed in an enclosed vacuum tank in order to adjust the pressure so that the Reynolds number can be controlled while having the same rotational speed. First, a validation experiment has been performed to verify the correct working of the set-up. For two different airfoils, consequently, the thrust and power (coefficient) is computed at different Reynolds numbers. Using the Blade Element Momentum Theory, the thrust and power (coefficient) is also computed under the same circumstances. The experimental data coincide with the used theory fairly well for pitch angles up to 20 degrees for both airfoils. The reason for this deviation from 20 degrees pitch angle is stall of the blades. This is not captured in the theory. In practice, the blades will operate below stall angles which makes the theory suitable for the final design. In the future, experiments will be performed to increase the accuracy of the conceptual design program. The conceptual design program can be improved by taking into account the Mach number effect. Also, the correct interference factor in coaxial flight will be computed. Finally, the pitch difference between lower and upper rotor to assure torque balance will be examined.

As future work, the conceptual design program should be extended by incorporating forward flight. Also, CFD calculations are planned to be performed to validate the final design and to see the occurring flow phenomena. It is expected that with these CFD calculations, the tip and hub shape can be improved in order to consume less power and to have a better estimation of the total power usage including fuselage. Besides the aerodynamic performance, the structural strength and blade dynamics should also be researched.

Bibliography

[1] J Jones, S Saunders, J Blamont, and A Yavrouian. Balloons for controlled roving/landing on mars. *Acta astronautica*, 45(4-9):293–300, 1999.

[2] VV Kerzhanovich, JA Cutts, HW Cooper, JL Hall, BA McDonald, MT Pauken, CV White, AH Yavrouian, A Castano, HM Cathey Jr, et al. Breakthrough in mars balloon technology. *Advances in Space Research*, 33(10):1836–1841, 2004.

[3] R Braun, H Wright, M Croom, and D Levine, Jand Spencer. Design of the ares mars airplane and mission architecture. *Journal of Spacecraft and Rockets*, 43(5):1026–1034, 2006.

[4] S Smith, A Hahn, W Johnson, D Kinney, J Pollitt, and J Reuther. The design of the canyon flyer, an airplane for mars exploration. In *38th Aerospace Sciences Meeting and Exhibit*, page 514, 2000.

[5] K Fujita, R Luong, H Nagai, and K Asai. Conceptual design of mars airplane. *transactions of the Japan society for aeronautical and space sciences, aerospace technolgy*, 10(28), 2012.

[6] I Chopra, V Hrishikeshavan, R Shrestha, and M Benedict. Hover performance of a small-scale helicopter rotor for flying on mars. Technical report, University of Maryland & Texas A&M University, 2018.

[7] A Datta, I Chopra, J Bao, O Gamard, D Griffiths, L Liu, G Pugliese, B Roget, and J Sitamaran. The martian autonomous rotary-wing vehicle (marv). *Alfred Gessow Rotorcraft Center, Department of Aerospace Engineering, University of Maryland, College Park, Maryland*, 1, 2000.

[8] LA Young, EW Aiken, V Gulick, R Mancinelli, and GA Briggs. Rotorcraft as mars scouts. In *Aerospace Conference Proceedings, 2002. IEEE*, volume 1, pages 1–378. IEEE, 2002.

[9] M Lacerda, D Park, S Patel, and D Schrage. A preliminary systems engineering study on a concept for mars exploration with an unmanned autonomous vehicle and ground rover configuration. Technical report, Georgia University of Technology, 2018.

[10] Witold J.F. Koning, Ethan A. Romander, and Wayne Johson. Low reynolds number airfoil evaluation for the mars helicopter rotor. Technical report, NASA AMES research center, 2018.

[11] R Aoki, A Oyama, K Fujita, H Nagai, M Kanazaki, K Kanou, N Inoue, S Sokabe, K Tomisawa, and K Uwatoko. Conceptual helicopter design for exploration of pit craters and caves on mars. In *AIAA SPACE and Astronautics Forum and Exposition*, page 5362, 2018.

[12] M Okochi. Experimental study of rotor performance at low reynolds number conditions. *Transactions of the JSASS*, 44:6p, 2013.

[13] A Gessow. Effect of rotor-blade twist and plan-form taper on helicopter hovering performance. 1948.

[14] A Nikolsky. *Helicopter analysis.* Wiley, 1951.

[15] F Lucas. Study of contra-rotating coaxial rotors in hover, a performance model based on blade element theory including swirl velocity. 2007.

[16] L Prandtl and A Betz. *Vier Abhandlungen zur Hydrodynamik und Aerodynamik*, volume 3. Universitätsverlag Göttingen, 2010.

[17] G Leishman. *Principles of helicopter aerodynamics 2nd edition.* Cambridge University press, 2006.

[18] R Harrington. Full-scale-tunnel investigation of the static-thrust performance of a coaxial helicopter rotor. 1951.

[19] H Snel, R Houwink, J Bosschers, et al. *Sectional prediction of lift coefficients on rotating wind turbine blades in stall.* Netherlands Energy Research Foundation Petten, Netherlands, 1994.

[20] H Hidaka and M Okamoto. An experimental study of triangular airfoils for mars airplane. *Transactions of the JSASS*, 12(29):21–27, 2014.

[21] Hermann Glauert. The effect of compressibility on the lift of an aerofoil. *Proc. R. Soc. Lond. A*, 118(779):113–119, 1928.

[22] M Anyoji, D Numata, H Nagai, and K Asai. Effects of mach number and specific heat ratio on low-reynolds-number airfoil flows. *AIAA Journal*, 53(6):1640–1654, 2014.

[23] Seika Mikrosystemtechnik GmbH. *Inclinometer NA3-30.* Available at `http://www.seika.de/english/pdf_e/NA_e.pdf`.

[24] Omron Industrial Automation. *E3Z-T61 Through-Beam NPN.* Available at `http://www.mouser.com/ds/2/307/D04E3Z1204-27342.pdf`.

[25] Maxon Motor. *Escon Studio 2.2.* Available at `https://www.maxonmotor.com/maxon/view/content/ESCON-Detailsite`.

[26] Maxon Motor. *Datasheet Maxon RE35 graphite brushed DC motor.* Available at `https://www.maxonmotor.com/medias/sys_master/root/8830469668894/2018EN-130.pdf`.

Chapter 5

Appendix 1: Input values flowchart

Table 5.1: Input values Mars atmosphere

Parameter	Value	Unit
Air density	0.017847	$[kg/m^3]$
Speed of sound	220	$[m/s]$
Gravitational constant	3.711	$[m/s^2]$
Viscosity	1.4e5	$[Pas]$

Table 5.2: Input values blades & hub

Parameter	Value	Unit
Number of disks	2	[-]
Number of blades	2-2	[-]
Radius	1	$[m]$
Pitch angle	12	$[deg]$
Blade thickness ratio (t/c)	0.01	[-]
Hub thickness	0.005	[m]
Wingtip Mach number	0.8	[-]
Ratio hub radius to rotor radius	0.1	[-]

Table 5.3: Input values masses

Parameter	Value	Unit
Rotor density	1800	$[kg/m^3]$
Hub density	1500	$[kg/m^3]$
Motor power density	2000	$[W/kg]$
Battery energy density	200	$[Wh/kg]$
Cable mass ratio (divided by total kg)	0.03	[-]
Margin mass ratio (divided by equipment mass)	0.3	[-]
Body structure mass	0.360	$[kg]$
Equipment mass	1.03	$[kg]$

Table 5.4: Input values general

Parameter	Value	Unit
Thrust margin	1.1	[-]
Battery margin	1.1	[-]
Efficiency motor	0.8	[-]
Wake interference factor	1.16	[-]

Chapter 6

Appendix 2: Vacuum tunnel test stand

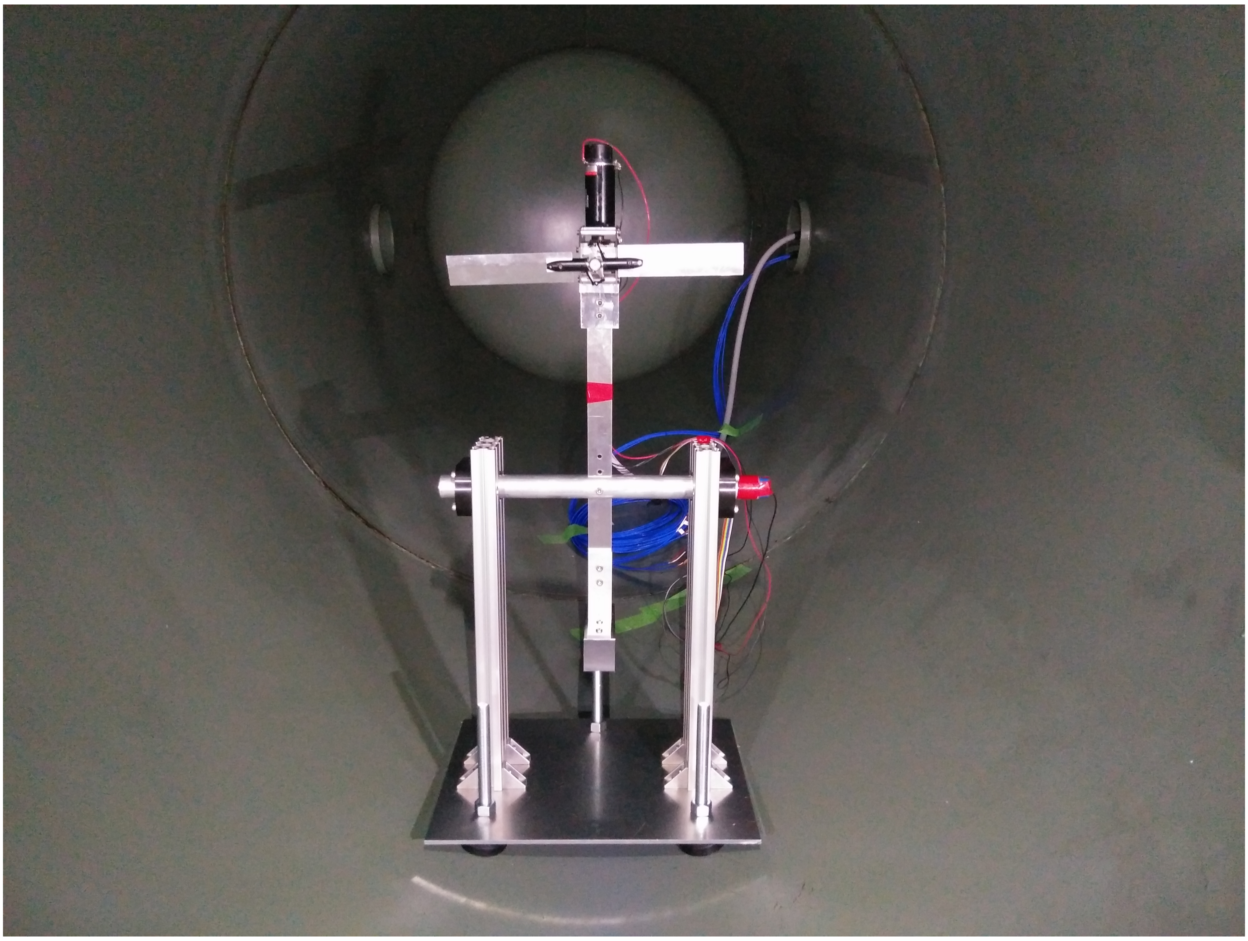

Figure 6.1: Pendulum test stand inside vacuum tunnel - Front

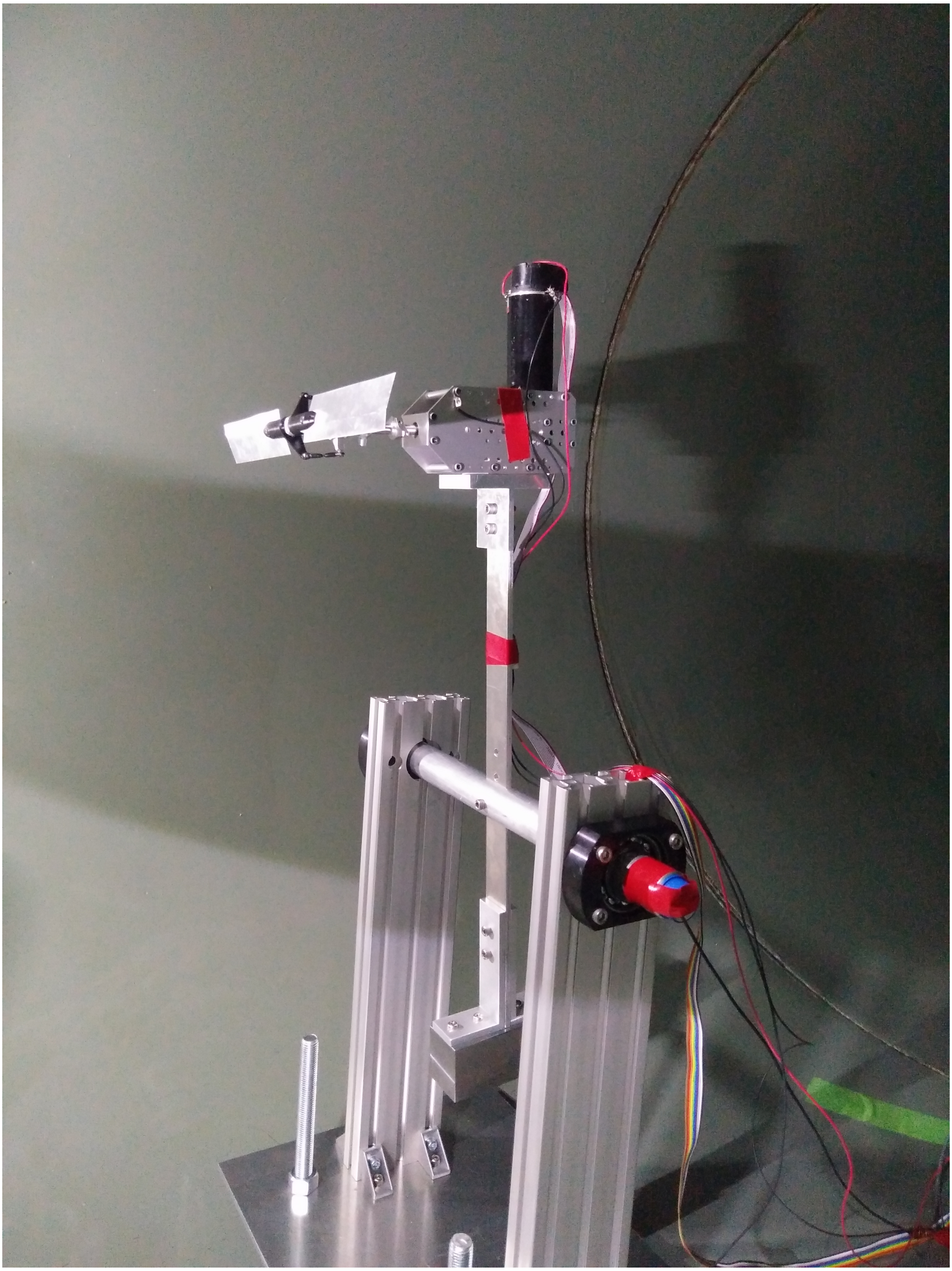

Figure 6.2: Pendulum test stand inside vacuum tunnel - Side